Lie Meng[1]
Jing-Cai Cheng[2]
Hong Jiang[1]
Chao Yang[2]
Wei-Hong Xing[1]
Wan-Qin Jin[1]

[1] Nanjing University of Technology, College of Chemistry and Chemical Engineering, State Key Laboratory of Materials-Oriented Chemical Engineering, Nanjing, China.

[2] Chinese Academy of Sciences, Institute of Process Engineering, Key Laboratory of Green Process and Engineering, Beijing, China.

Research Article

Design and Analysis of a Submerged Membrane Reactor by CFD Simulation

CFD was applied to demonstrate the effect of reactor configurations on the fluid flow pattern in submerged membrane reactors. A mixture model, a realizable k-ε model, and the multiple reference frame (MRF) technique were employed to simulate the solid-liquid turbulent flow. Influences of the introduction of a ceramic membrane, the relative position between ceramic membrane and impeller, and the types of impeller on velocity profiles and concentration distributions were systematically discussed. These simulation results were validated qualitatively with experimental data for various reactor configurations.

Keywords: Computational fluid dynamics, Phenol hydroxylation, Porous ceramic membrane, Submerged membrane reactor

Received: March 27, 2013; *revised:* July 07, 2013; *accepted:* August 09, 2013

DOI: 10.1002/ceat.201300206

1 Introduction

As a novel chemical reactor configuration, the submerged membrane reactor, which couples the catalytic reaction with membrane separation, can effectively solve the problem concerning ultrafine catalyst recovery in industrial production [1]. Our previous researches indicated an impressive performance of the submerged membrane reactor in heterogeneous catalysis such as phenol hydroxylation and *p*-nitrophenol hydrogenation [2–6]. Owing to the introduction of ceramic membranes, both the reaction conversion and product selectivity were obviously improved while nearly no weight loss of catalyst particles could be noticed. The submerged membrane reactor also had other advantages like low energy consumption and small footprint which were favored by the chemical industry.

In membrane separation processes, the hydrodynamics has a significant influence on the membrane performance, e.g., the velocity distribution on the membrane surface is correlated with the membrane flux in the case of a solid-liquid system [7]. However, the flow field in the submerged membrane reactor can affect the distribution of solid catalyst particles, thus producing a distinct impact on reaction conversion and product selectivity. To optimize the design and configuration of a submerged membrane reactor, it is essential to systematically study the flow field inside such a reactor. Some researchers have adopted a general practice to evaluate the performance of a membrane reactor through experimental investigation [8–10]. However, it is difficult to obtain the flow field distribution in the whole membrane reactor by experimental measurements. Such an approach is usually time-consuming, costly, and sometimes impractical. Recently, numerical simulation of the processes involved with membrane separation has received considerable attention due to its ability in finding the optimum condition for an operational system under study [11–14]. Vigneault et al. [14] developed a steady-state 2D model for a multichannel membrane reactor to produce pure hydrogen, and their predictions indicated that the reforming methane conversion increased from 74 to 91 % after optimization.

Nowadays, on the reactor scale, CFD is a widely used simulation tool for investigating and predicting the performance of processes involved with flow, heat, and mass transfer [15, 16]. This method has opened the gate to visualize the flow field distribution in a multiphase system without conducting real-time experiments and to provide in-depth details about the fluid flow which may not be available from practical approaches [17–19]. Consequently, CFD has been applied in the membrane separation technology for process optimization [20, 21]. Ghidossi et al. reviewed some published works on CFD simulations of membrane separations [22]. They showed that CFD can provide interesting and important information about the development of membrane processes.

Concerning the membrane transport phenomena, Wiley and Fletcher [23] employed a CFD model to describe the pressure-driven membrane processes. They found that fine meshes near the membrane wall, high-order numerical schemes, accurate modeling of rejection, and the physical property variations were essential for accurate and reliable

Correspondence: Prof. W. Q. Jin (wqjin@njut.edu.cn), Nanjing University of Technology, College of Chemistry and Chemical Engineering, State Key Laboratory of Materials-Oriented Chemical Engineering, 5 Xinmofan Road, Nanjing 210009, China.

predictions. For optimizing the membrane process, Brannock et al. [24, 25] developed a CFD model taking aeration and the membrane configuration into account. They concluded that aeration was the main mixing mechanism, and the inlet position might not greatly influence the internal recirculation but could bring the system closer to complete mixing.

Although the submerged membrane reactor already has been used in heterogeneous catalytic reactions, its design and optimization are still mainly based on reaction kinetics and membrane fouling considerations. More importantly, two key factors, i.e., the velocity distribution on the membrane surface and the concentration distribution of catalysts are difficult to directly obtain by experimental means. In this paper, CFD was used to predict the fluid flow pattern in a solid-liquid stirred submerged membrane reactor. The influence of the introduction of a ceramic membrane, the relative position between ceramic membrane and impeller, and the types of impeller on velocity profiles and concentration distributions in a stirred submerged membrane reactor was systematically discussed. The simulation results are in reasonable agreement with our experimental data.

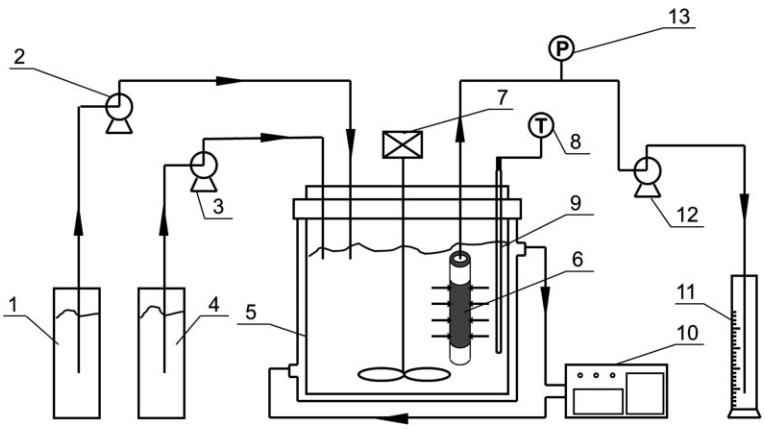

Figure 1. Submerged membrane reactor: (1) hydrogen peroxide solution storage tank, (2) hydrogen solution feed pump (constant flow pump), (3) phenol solution feed pump (peristaltic pump), (4) phenol solution storage tank, (5) reactor, (6) membrane module, (7) stirrer, (8) temperature controller, (9) thermocouple, (10) water bath, (11) reaction mixture receiver, (12) discharge pump (peristaltic pump), (13) vacuum gauge.

Table 1. Design parameters and physical properties of the submerged membrane reactor.

Geometry	Physical properties	Operating conditions
$T = 0.14$ m, $H = 0.15$ m	Liquid: $\rho = 1100\ \mathrm{kg\,m^{-3}}$	Solid concentration = 0.1 wt %
$D = 0.05$ m, $C/T = 0.2$	Solid: $\rho = 2230\ \mathrm{kg\,m^{-3}}$	$N = 380$ rpm
	$d_s = 300$ nm	

2 Experimental

2.1 Submerged Membrane Reactor

A submerged ceramic membrane reactor system was constructed and is presented schematically in Fig. 1. It consisted mainly of a slurry stirred reactor, ceramic membrane module, feed system, and heating system. The reactor was a transparent cylindrical tank with a flat bottom, had an internal diameter of $T = 0.14$ m, and was filled with a liquid up to $H = 0.15$ m. One end of the tubular ceramic membrane was sealed with a glazing compound while the other end served as the liquid outlet. A constant-flow pump (Beijing Chuangxin Tongheng Science & Technology Co., Ltd., China) was employed to feed H_2O_2 into the phenol solution which ensured a steady flow rate of H_2O_2. The reactor was immersed in a water bath whose temperature was controlled by a temperature controller (Shanghai Hua Chen Medical Instruments, China).

The dimensions of the membrane reactor and the physical properties of all the phases considered are given in Tab. 1. The liquid phase was the reaction liquid and the solid phase for the present study referred to the solid catalyst particles with a mean diameter of 300 nm and a loading of 0.1 wt %. Three types of pitched-blade impellers, i.e., with two blades, three blades, and four blades, respectively, were considered. The impellers with the same diameter $D = T/3$ were used, and clearance (C) between impeller and tank bottom was selected as $C = T/5$. The rotation speed was set to $N = 380$ rpm.

2.2 Materials

The tubular ceramic membrane was provided by Nanjing Jiusi High-Tech Co., Ltd., China, and its effective length, outer diameter, and inner diameter were 60, 12, and 8 mm, respectively. Phenol and hydroquinone were purchased from Shantou Xilong Chemical Co., Ltd. (China). Catechol was provided by the Shanghai Sansi Reagent Co., Ltd. (China), and 30 % H_2O_2 solution was supplied by the Sinopharm Chemical Reagent Co., Ltd. (China). The above materials were of analytical grade. Methanol (> chromatography grade) was from the Yuwang Group (China). The TS-1 catalyst (300 nm average particle size) was provided by Baling Petrochemical Co. (China). All water used in this work was self-prepared deionized water and had an electrical conductivity below 12 $\mu S\ cm^{-1}$.

2.3 Hydroxylation Experiment

For comparison with the simulation results, phenol hydroxylation with hydrogen peroxide over TS-1 was performed in the submerged ceramic membrane reactor. For phenol hydroxylation catalyzed by TS-1, as a typical catalytic reaction in a solid-liquid system, the surface titanium peroxo compounds form with H_2O_2 and subsequently transfer the peroxidic oxygen to phenol [26, 27]. However, some unexpected by-products such as benzoquinone would be generated because of the strong

oxidizing properties of H_2O_2, resulting in the decrease of dihydroxybenzene (DHB) selectivity, as depicted in Fig. 2.

After given amounts of phenol aqueous solution and TS-1 catalyst were added into the reactor, the system was heated to 353 K under stirring. When the temperature reached the set value, 30 % H_2O_2 solution was added into the phenol solution at a certain flow rate. After reacting for 60 min, the phenol aqueous solution and H_2O_2 solution were fed continuously into the reactor at a total flow rate of 2 mL min^{-1}. The products were taken out with a peristaltic pump at a flow rate of 2 mL min^{-1} which equals to the total feeding flow rate. The operation pressure of the membrane separation was monitored by a vacuum gauge. The reaction products were analyzed by HPLC (Agilent 1100 Series, USA) equipped with a diode array detector, an autosampler, and a Zorbax Eclipse XDB-C18 column. The analyses were performed at 308 K by a UV detector at 277 nm using a mobile phase consisting of methanol/pure water (40:60 v/v) at a flow rate of 1 mL min^{-1}. The automatic injection volume was 5 μL per sample. A calibration curve of oxidation products was drawn using aqueous samples of known composition. Phenol conversion and dihydroxybenzene (DHB) selectivity were calculated on the basis of the starting amount of phenol, according to Eqs. (1) and (2), respectively [6].

$$X = \frac{C_{\text{phenol(o)}} - C_{\text{phenol(p)}}}{C_{\text{phenol(o)}}} \tag{1}$$

$$S = \frac{C_{\text{CA}} + C_{\text{HQ}}}{C_{\text{phenol(o)}} - C_{\text{phenol(p)}}} \tag{2}$$

where X is the phenol conversion, S is the DHB selectivity, $C_{\text{phenol(o)}}$ is the initial phenol concentration in the feed (mol L^{-1}), $C_{\text{phenol(p)}}$ is the phenol concentration in the outlet of the reactor (mol L^{-1}), and C_{CA} and C_{HQ} are the concentrations of catechol and hydroquinone in the outlet of the reactor (mol L^{-1}), respectively. To achieve reproducible results, multiple (more than triplicate) experiments were mostly performed and are presented with error bars.

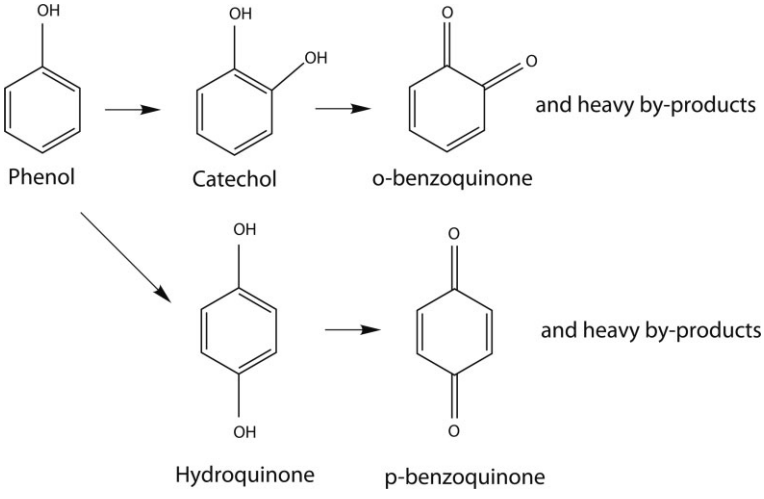

Figure 2. Hydroxylation of phenol with hydrogen peroxide over a TS-1 catalyst.

3 Computational Details

3.1 Mathematical Model

A simplified multiphase model, i.e., the mixture model, is employed to simulate the solid-liquid flow. Applying the conservation laws of mass and momentum for the mixture phase, the resulting conservation equations for phase q can be written as follows:

Continuity equation for the mixture:

$$\frac{\partial}{\partial t}(\rho_{\text{m}}) + \nabla \bullet (\rho_{\text{m}} \mathbf{u}_{\text{m}}) = 0 \tag{3}$$

where ρ_{m} denotes the mixture density which is defined by:

$$\rho_{\text{m}} = \sum_{\text{q}=1}^{\text{n}} \alpha_{\text{q}} \rho_{\text{q}} \tag{4}$$

where ρ_{q} and α_{q} are the density and volume fraction of the qth phase, respectively. The mass-averaged velocity $\mathbf{u}_{\text{m}}$ is defined by:

$$\mathbf{u}_{\text{m}} = \frac{\sum_{\text{q}=1}^{\text{n}} \alpha_{\text{q}} \rho_{\text{q}} \mathbf{u}_{\text{q}}}{\rho_{\text{m}}} \tag{5}$$

The momentum equation for the mixture can be obtained by summing the individual momentum equations for all phases and can be expressed as:

$$\frac{\partial}{\partial t}(\rho_{\text{m}} \mathbf{u}_{\text{m}}) + \nabla \bullet (\rho_{\text{m}} \mathbf{u}_{\text{m}} \mathbf{u}_{\text{m}}) = -\nabla p + \nabla \bullet \tau_{\text{m}} + \rho_{\text{m}} \mathbf{g} + \mathbf{F} + \nabla \bullet \left(\sum_{\text{q}=1}^{\text{n}} \alpha_{\text{q}} \rho_{\text{q}} \mathbf{u}_{\text{dr,q}} \mathbf{u}_{\text{dr,q}} \right) \tag{6}$$

where $\mathbf{F}$ is the body force, $\mathbf{u}_{\text{dr,q}}$ is the drift velocity for the secondary phase q, $\mathbf{u}_{\text{dr,q}} = \mathbf{u}_q - \mathbf{u}_{\text{m}}$, and τ_{m} is the mixture phase stress-strain tensor, $\tau_{\text{m}} = \mu_{\text{m}}(\nabla \mathbf{u}_{\text{m}} + \nabla \mathbf{u}_{\text{m}}{}^{\text{T}})$. The definition of the mixture viscosity μ_{m} is very similar to that of ρ_{m}.

$$\mu_{\text{m}} = \sum_{\text{q}=1}^{\text{n}} \alpha_{\text{q}} \mu_{\text{q}} \tag{7}$$

The drift velocity for the secondary phase (i.e., the solid phase) $\mathbf{u}_{\text{dr,s}}$ is expressed by:

$$\mathbf{u}_{\text{dr,s}} = \mathbf{u}_{\text{sl}} - \sum_{\text{q}=1}^{\text{n}} \frac{\alpha_{\text{q}} \rho_{\text{q}} \mathbf{u}_{\text{lq}}}{\rho_{\text{m}}} \tag{8}$$

where $\mathbf{u}_{\text{sl}}$ is the slip velocity defined as the velocity of the solid phase; $\mathbf{u}_{\text{s}}$ is relative to the velocity of the continuous phase $\mathbf{u}_{\text{l}}$, $\mathbf{u}_{\text{sl}} = \mathbf{u}_{\text{s}} - \mathbf{u}_{\text{l}}$. The slip velocity can be expressed by an algebraic relation:

$$\mathbf{u}_{\text{sl}} = \frac{\tau_{\text{s}}}{f_{\text{drag}}} \frac{(\rho_{\text{s}} - \rho_{\text{m}})}{\rho_{\text{s}}} \mathbf{a} \tag{9}$$

where τ_{s} is the solid particle relaxation time:

$$\tau_{\text{s}} = \frac{\rho_{\text{s}} d_{\text{s}}^2}{18 \mu_{\text{l}}} \tag{10}$$

and $\mathbf{a}$ is the secondary-phase particle's acceleration:

$$\mathbf{a} = \mathbf{g} - (\mathbf{u}_m \bullet \nabla)\mathbf{u}_m - \frac{\partial \mathbf{u}_m}{\partial t} \quad (11)$$

The simplest algebraic slip formulation is the so-called drift flux model, in which the acceleration of the particle is given by gravity and/or a centrifugal force and the particulate relaxation time is modified to take into account the presence of other particles.

The modeled transport equations for k and ε in the realizable k-ε model are:

$$\frac{\partial}{\partial t}(\rho k) + \frac{\partial}{\partial x_j}(\rho k u_j) = \frac{\partial}{\partial x_j}\left[\left(\mu + \frac{\mu_t}{\sigma_k}\right)\frac{\partial k}{\partial x_j}\right] + G_k + G_b - \rho\varepsilon - Y_M + S_k \quad (12)$$

and

$$\frac{\partial}{\partial t}(\rho\varepsilon) + \frac{\partial}{\partial x_j}(\rho\varepsilon u_j) = \frac{\partial}{\partial x_j}\left[\left(\mu + \frac{\mu_t}{\sigma_\varepsilon}\right)\frac{\partial \varepsilon}{\partial x_j}\right] + \rho C_1 S_\varepsilon - \rho C_2 \frac{\varepsilon^2}{k + \sqrt{\nu\varepsilon}} + C_{1\varepsilon}\frac{\varepsilon}{k}C_{3\varepsilon}G_b + S_\varepsilon \quad (13)$$

where

$$C_1 = \max\left[0.43, \frac{\eta}{\eta + 5}\right], \eta = S\frac{k}{\varepsilon}, S = \sqrt{2S_{ij}S_{ij}} \quad (14)$$

3.2 CFD Simulation

Fluent 6.3 (Ansys Inc., USA) was used to simulate the mixing of the solid-liquid system in the submerged membrane reactor. The first step is the grid generation which divides the calculation domain into discrete control volumes. Gambit 2.4 (Ansys Inc., USA) is applied to divide the flow domain into a certain number of tetrahedral cells. The advantage of an unstructured grid is that a complex geometry (e.g., the impeller) can be meshed easily. All the generated grids are of a skewness below 0.9 which indicates an acceptable mesh quality. The numerical simulations for solid-liquid flows in the stirred submerged membrane reactor were carried out with grid elements of 300 000–400 000. The multiple reference frame (MRF) technique is employed to treat the interaction between the rotating impeller and the stationary membrane reactor. A rotating frame having the same rotational speed as the impeller is used for the inner region and a stationary frame for the outer region. During the solution process, a steady transfer of information occurs across a predefined interface between the two frames. The inner region is a cylinder of 10 cm in diameter and 5 cm in height and is centered on the impeller. The shaft of the impeller is not included in this inner region. This method facilitates the incorporation of the impeller motion even with a complex geometry.

No-slip and no-penetration conditions are imposed on the reactor walls. Symmetric boundary conditions, i.e., the zero normal velocity and zero normal gradients for all variables, are assumed on the liquid surface. Since the shear stress is zero at the symmetric boundary, it is also called the slip wall boundary condition. The wall boundary condition is applied to the shaft of the impeller and the inner wall of the reactor. Standard wall functions are used to specify the wall boundary conditions. The local solid concentrations were monitored during the simulations. Simulations are considered to be converged when the fluctuations of the solid concentrations in the membrane reactor are inconspicuous, and the scaled residuals for all transport equations are below 10^{-4}.

4 Results and Discussion

4.1 Effect of Introduction of a Ceramic Membrane

Firstly, CFD simulations were performed to investigate the flow fields in the submerged membrane reactor, and the predictions in the case without a ceramic membrane were also presented for comparison. As can be seen clearly from Fig. 3,

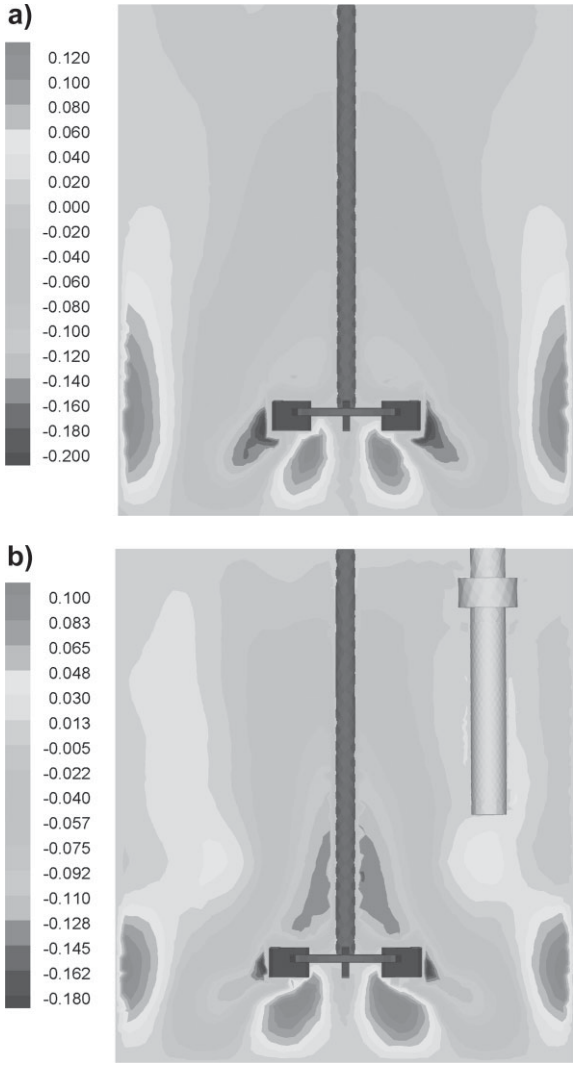

Figure 3. Contours of Z velocity ($m\,s^{-1}$) predicted in the submerged membrane reactor in cases of (a) without and (b) with a ceramic membrane.

the introduction of a ceramic membrane distinctly affected the bulk flow patterns and as a result the axial flow in the submerged membrane reactor was strengthened, which could strongly influence the distribution of solid catalyst particles. So it is necessary to study the effect of reactor configuration parameters, such as the position of the ceramic membrane and the types of impeller on the flow field distribution in the submerged membrane reactor.

4.2 Effect of Position between Impeller and Ceramic Membrane

In membrane separation processes, membrane fouling, which plays a significant role in the decline of permeate flux, is a key factor affecting the economic and commercial viability of a membrane system. To inhibit membrane fouling, one frequently used method is to increase the membrane surface velocity which effectively reduces fouling and then restores flux [28, 29]. However, it is difficult to directly measure the membrane surface velocity through experimental methods. The investigation of membrane fouling was mainly based on the obtained membrane permeate flux. In order to investigate the dependence of the reactor configuration on the membrane surface velocity, the velocity distribution in the solid-liquid stirred submerged membrane reactor was calculated by CFD simulation and compared with the membrane permeate flux obtained from experiments.

Fig. 4 a displays the experimentally measured membrane permeate flux and the predicted membrane surface velocity of variation at different distances between impeller and ceramic membrane. It can be observed that the membrane permeate flux decreased as the distance between impeller and ceramic membrane became larger. The same trend can also be found in terms of the simulated velocity distribution on the membrane surface which implied a good agreement between our CFD simulations and experiments. Fig. 4 b exhibits the phenol conversion and DHB selectivity of variation at different distances between impeller and ceramic membrane. The phenol conversion gradually increased as the ceramic membrane was placed closer to the impeller, while the DHB selectivity remained the same. As mentioned above, in the submerged membrane reactor, a closer distance between the impeller and the ceramic membrane was in favor of higher membrane surface velocity. A higher membrane surface velocity reduced the thickness of the membrane fouling layer, and thus the adsorption amount of catalysts on the membrane surface decreased which kept the catalyst concentration in the reaction system constant. Therefore, a closer distance between the impeller and the ceramic membrane could result in an improvement of phenol conversion by promoting the homogeneity of catalyst particles distribution within the membrane reactor.

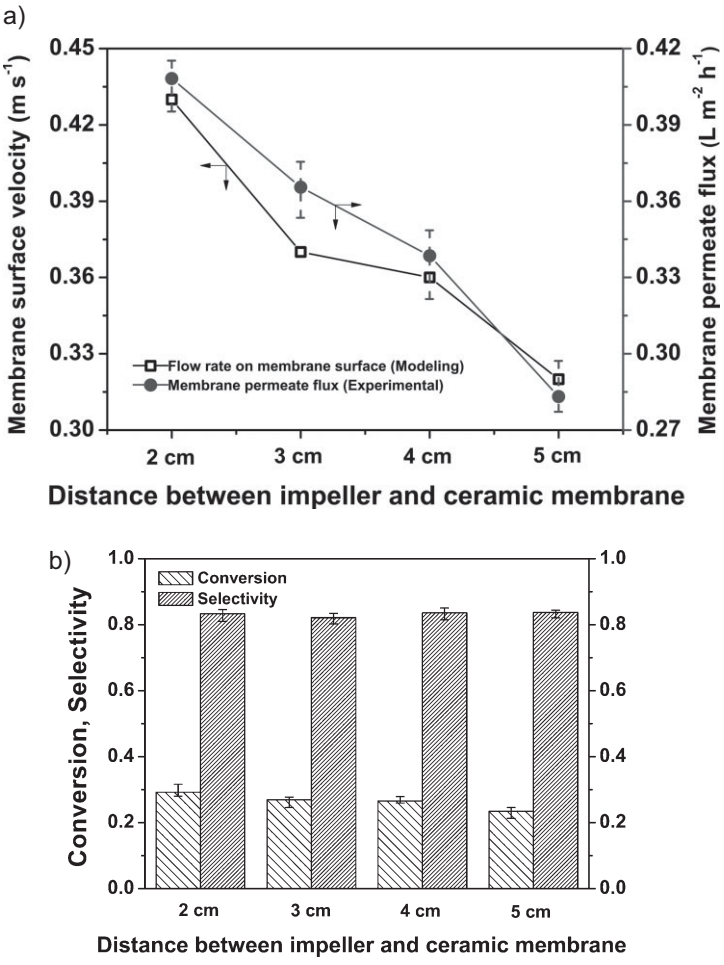

Figure 4. (a) Experimentally measured membrane permeate flux and predicted membrane surface velocity of variation at different distances between impeller and ceramic membrane; (b) phenol conversion and DHB selectivity of variation at different distances between impeller and ceramic membrane.

4.3 Effect of Impeller Design

The impeller is the core component of the submerged membrane reactor, and the velocity distribution and the concentration field are both closely related to the impeller type. For heterogeneous catalysis, usually axial impellers are chosen because they create an effective pumping and generate larger bulk recirculation which is favored by the solid-liquid suspension. They are also claimed to produce smaller shear effects than radial propellers [30]. In order to understand the quantitative role of the impeller design, CFD simulations were conducted for three impeller types which differed in the blade numbers (two, three, and four blades). Fig. 5 a illustrates the simulated membrane surface velocity for these three different impeller types which is compared with the membrane permeate flux obtained from experiments. The membrane surface velocity in the case of the three-blade and four-blade impellers was higher than that of the two-blade impeller which was consistent with the measured membrane

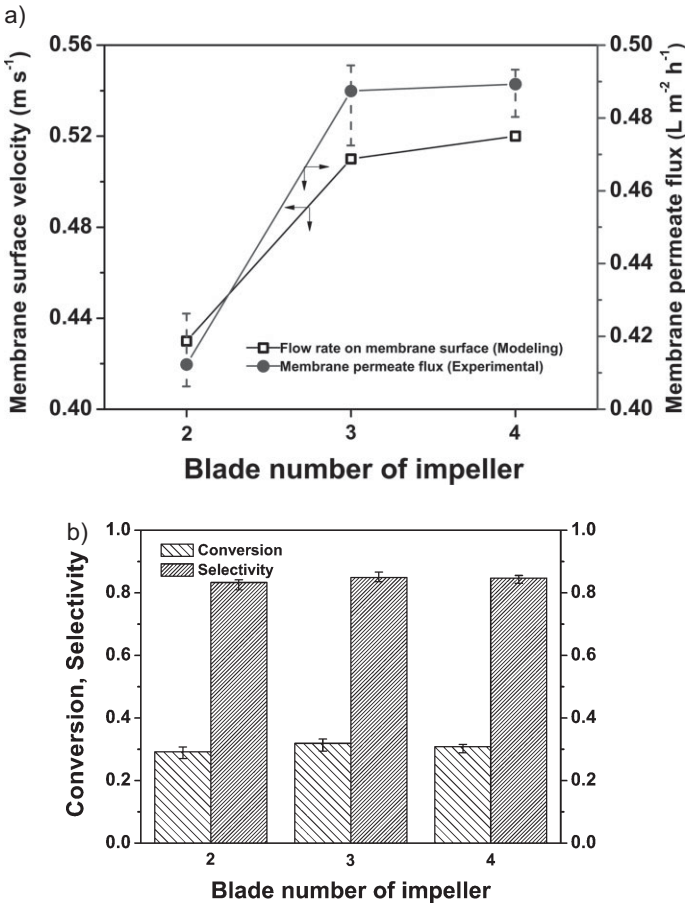

Figure 5. (a) Experimentally measured membrane permeate flux and predicted membrane surface velocity with different impeller blade numbers; (b) effect of impeller blade number on phenol conversion and DHB selectivity.

permeate flux. This was possibly because the impeller with more blades could create a higher cross-flow shear stress along the membrane surface. Fig. 5 b displays the influence of blade number of impeller on phenol conversion and DHB selectivity. For the two-blade impeller, phenol conversion and DHB selectivity were much lower than those of the three-blade and four-blade impellers which agreed well with the numerical simulation.

In order to further optimize the design of an impeller to maximize the performance of the submerged membrane reactor, the three-blade impellers with different blade angles ($\theta = 0°$, 30°, 45°, and 60°) were investigated. Fig. 6 depicts the concentration fields of TS-1 particles in the submerged membrane reactor. The 0° pitch three-blade impeller exhibited a lower degree of homogeneity which meant the weak solid-phase dispersion ability, as indicated in Fig. 6 a. The maximum homogeneity of solid particles was achieved at $\theta = 30°$, and a further increase in the impeller blade pitch angle caused a slight decrease in the homogeneity within the membrane reactor. It should also be noted that the amount of TS-1 solid particles, which settled at the bottom of the submerged membrane reactor, marginally increased while the blade pitch angle became larger.

Fig. 7 a illustrates the simulated velocity on the ceramic membrane surface and the measured membrane permeate flux in the case of different blade pitch angles. The velocity on the ceramic membrane surface decreased with an increase in the blade pitch angle. The reduction of velocity was attributed to the enhanced turbulence and energy dissipation in the submerged membrane reactor with larger blade pitch angles (see Fig. 8).

Fig. 7 b presents phenol conversion and DHB selectivity acquired on the basis of four impellers with different blade angles. Both phenol conversion and DHB selectivity were found to first rise as the blade angle increased, reached a maximum value, and then dropped. These trends fitted the calculated concentration distribution of TS-1 catalytic particles which proved that CFD simulation is a meaningful tool for membrane reactor design.

5 Conclusions

The solid-liquid flow in a stirred submerged membrane reactor was studied by the mixture model combined with the realizable k-ε turbulence model. CFD simulations revealed the influence of introducing a ceramic membrane to the submerged membrane reactor. On this basis, the optimum distance between the impeller and the ceramic membrane was found to be 2 cm in the current reactor configuration. Comparative studies of two-blade, three-blade, and four-blade impellers indicated that the three-blade impeller was most suitable for the systems with low solid loadings and small reaction volumes. Numerical simulations were further extended to investigate the effect of the blade pitch angle on the flow field in the reactor, and a 30° pitch three-blade impeller was selected as a potential candidate considering the solid concentration distribution, velocity on ceramic membrane surface, and energy dissipation. The results obtained from CFD simulations were validated qualitatively with the experimental investigations which clearly highlighted the capability of CFD in predicting the hydrodynamic characteristics in submerged membrane reactors.

Acknowledgment

This work was supported by the National Basic Research Program of China (No. 2009CB623406), the National Natural Science Foundation of China (Nos. 20990222, 21006047), and the National Science Fund for Distinguished Young Scholars (No. 21025627).

The authors have declared no conflict of interest.

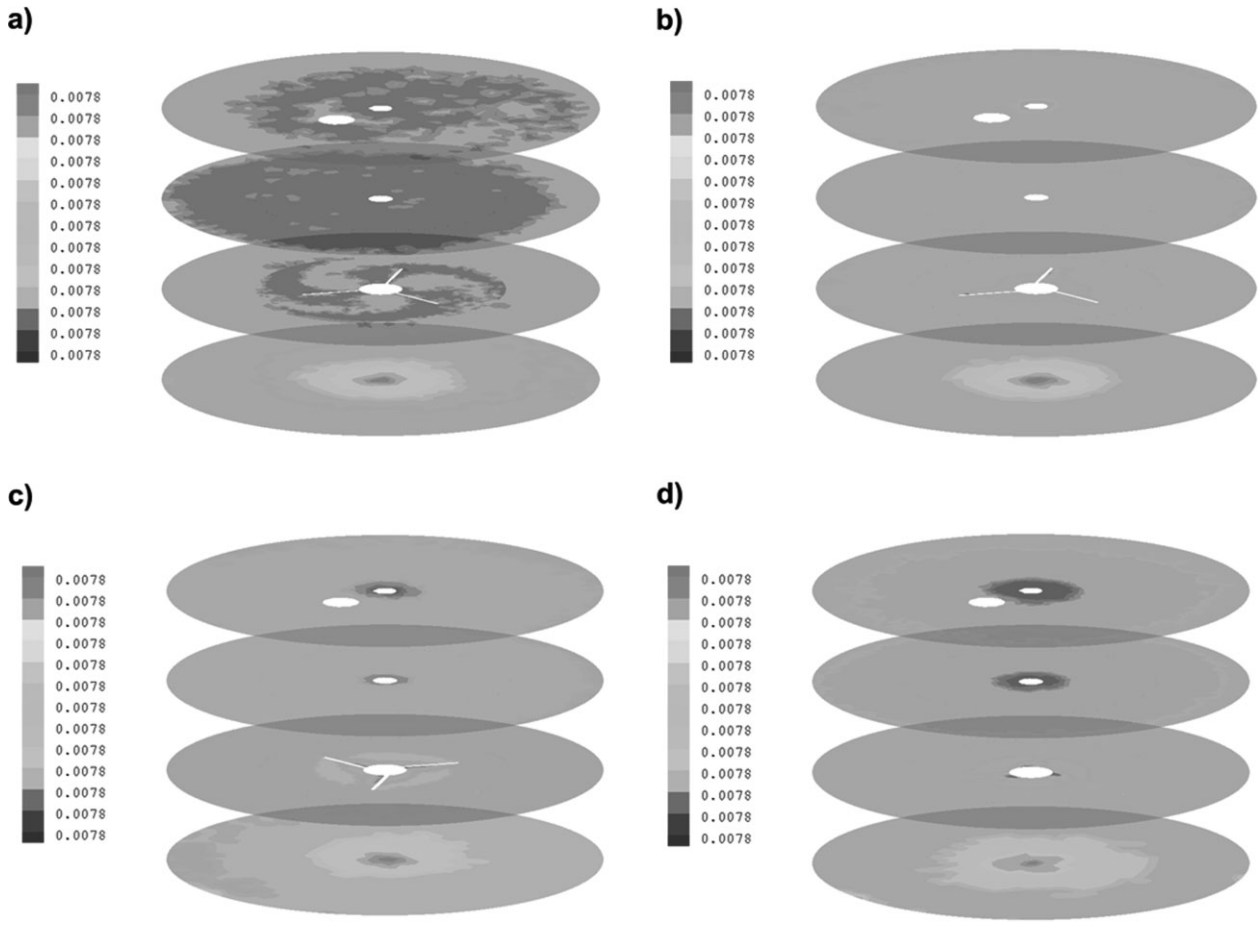

Figure 6. Concentration fields of TS-1 particles predicted in the submerged membrane reactor with (a) 0°, (b) 30°, (c) 45°, or (d) 60° pitch three-blade impellers.

Symbols used

a	[m s^{-2}]	acceleration
C	[m]	impeller off-bottom clearance
$C_{\mathrm{phenol(o)}}$	[mol L^{-1}]	phenol concentration in the feed
$C_{\mathrm{phenol(p)}}$	[mol L^{-1}]	phenol concentration in the outlet
C_{CA}	[mol L^{-1}]	catechol concentration in the outlet
C_{HQ}	[mol L^{-1}]	hydroquinone concentration in the outlet
D	[m]	impeller diameter
d_{s}	[nm]	particle diameter
F	[N]	body force
g	[m s^{-2}]	gravitational acceleration
H	[m]	liquid level
G_{k}	[kg m^{-1}s^{-3}]	generation of turbulence kinetic energy due to mean velocity gradients
G_{b}	[kg m^{-1}s^{-3}]	generation of turbulence kinetic energy due to buoyancy
k	[m^{2}s^{-2}]	turbulent kinetic energy
q	[–]	phase number
N	[rpm]	impeller speed
S	[–]	dihydroxybenzene selectivity
T	[m]	tank diameter
t	[s]	time
u	[m s^{-1}]	component of the flow velocity perpendicular to gravitational vector
u_{q}	[m s^{-1}]	phase k velocity
u_{sl}	[m s^{-1}]	slip velocity
u_{l}	[m s^{-1}]	liquid velocity
u_{s}	[m s^{-1}]	particle velocity
X	[–]	phenol conversion
Y_{M}	[kg m^{-1}s^{-3}]	fluctuating dilatation in compressible turbulence to overall dissipation rate

Greek letters

α_{q}	[–]	phase q volume fraction
ε	[m^{2}s^{-3}]	turbulent dissipation rate
θ	[°]	blade angle
μ	[Pa s]	viscosity
μ_{m}	[Pa s]	mixture viscosity
μ_{q}	[Pa s]	phase q viscosity
ν	[m^{2}s^{-1}]	kinematic viscosity of the liquid
ρ	[kg m^{-3}]	density
ρ_{q}	[kg m^{-3}]	phase q density
τ	[N m^{-2}]	shear stress
τ_{s}	[s]	solid particle relaxation time

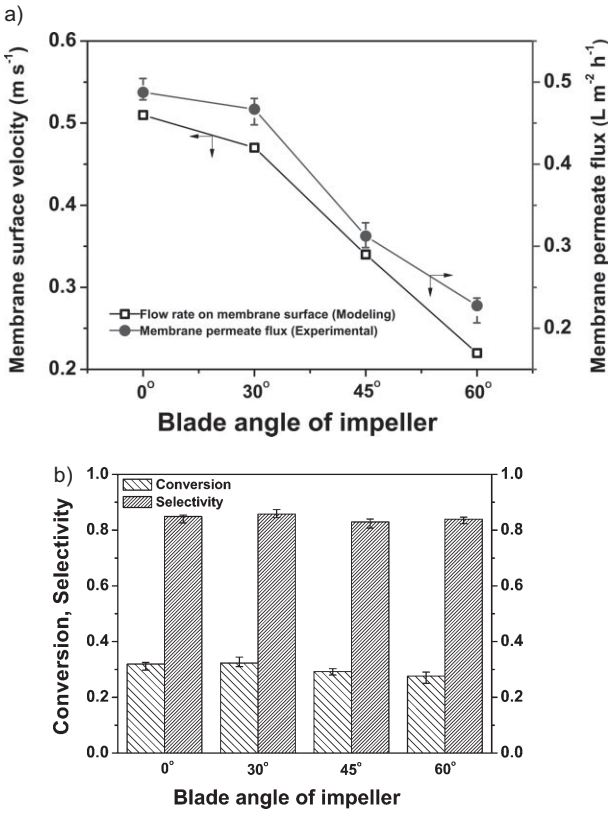

Figure 7. (a) Experimentally measured membrane permeate flux and predicted membrane surface velocity of variation at different impeller blade angles; (b) effect of impeller blade angles on phenol conversion and DHB selectivity.

References

[1] H. Jiang, L. Meng, R.-Z. Chen, W.-Q. Jin, W.-H. Xing, N.-P. Xu, *Chin. J. Chem. Eng.* **2013**, *21 (2)*, 205–215. DOI: 10.1016/S1004-9541 (13)60460-7

[2] C. Lu, R.-Z. Chen, W.-H. Xing, W.-Q. Jin, N.-P. Xu, *AIChE J.* **2008**, *54*, 1842–1849. DOI: 10.1002/aic.11514

[3] R.-Z. Chen, H. Jiang, W.-Q. Jin, N.-P. Xu, *Chin. J. Chem. Eng.* **2009**, *17*, 648–653. DOI: 10.1016/S1004-9541(08)60258-X

[4] R.-Z. Chen, Y. Du, Q.-Q. Wang, W.-H. Xing, W.-Q. Jin, N.-P. Xu, *Ind. Eng. Chem. Res.* **2009**, *48*, 6600–6607. DOI: 10.1021/ie900033m

[5] R.-Z. Chen, H.-L. Sun, W.-H. Xing, W.-Q. Jin, N.-P. Xu, *J. Nanosci. Nanotechnol.* **2009**, *9*, 1470–1473. DOI: 10.1166/jnn.2009.C181

[6] H. Jiang, L. Meng, R.-Z. Chen, W.-Q. Jin, W.-H. Xing, N.-P. Xu, *Ind. Eng. Chem. Res.* **2011**, *50*, 10458–10464. DOI: 10.1021/ie200398g

[7] Z. Li, R.-Z. Chen, W.-Q. Jin, W.-H. Xing, N.-P. Xu, *Ind. Eng. Chem. Res.* **2010**, *49*, 6309–6316. DOI: 10.1021/ie901912e

[8] J. K. Shim, I. K. Yoo, Y. M. Lee, *Process Biochem.* **2002**, *38*, 279–285. DOI: 10.1016/S0032-9592 (02)00077-8

[9] J. Zhang, H. C. Chua, J. Zhou, A. G. Fane, *J. Membr. Sci.* **2006**, *284*, 54–66. DOI: 10.1016/j.memsci.2006.06.022

[10] R.-Z. Chen, Y. Du, W.-H. Xing, W.-Q. Jin, *Korean J. Chem. Eng.* **2009**, *26*, 1580–1584. DOI: 10.1007/s11814-009-0273-9

[11] M. Kostoglou, A. J. Karabelas, *Ind. Eng. Chem. Res.* **2009**, *48*, 10025–10036. DOI: 10.1021/ie901129j

[12] M. Kostoglou, A. J. Karabelas, *Ind. Eng. Chem. Res.* **2011**, *50*, 4653–4666. DOI: 10.1021/ie102083j

[13] M. A. Rakib, J. R. Grace, C. J. Lim, S. S. E. H. Elnashaie, *Ind. Eng. Chem. Res.* **2011**, *50*, 3110–3129. DOI: 10.1021/ie100954a

[14] A. Vigneault, S. S. E. H. Elnashaie, J. R. Grace, *Chem. Eng. Technol.* **2012**, *35*, 1520–1533. DOI: 10.1002/ceat.201200029

[15] M. P. Dudukovic, *Science* **2009**, *325*, 698–701. DOI: 10.1126/science.1174274

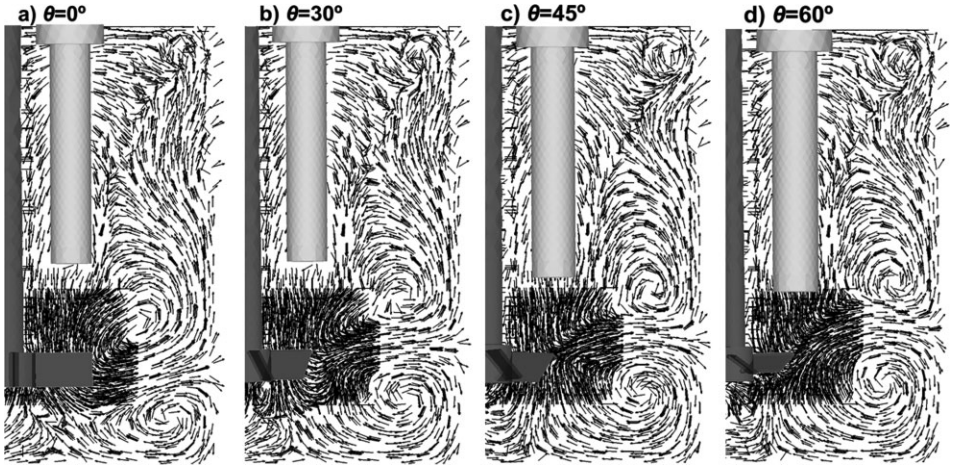

Figure 8. Effects of blade pitch angle on flow field predicted in the submerged membrane reactor with (a) 0°, (b) 30°, (c) 45°, or (d) 60° pitch three-blade impellers.

[16] M. P. Dudukovic, F. Larachi, P. L. Mills, *Catal. Rev.* **2002**, *44*, 123–246. DOI: 10.1081/CR-120001460
[17] J.-C. Cheng, C. Yang, Z.-S. Mao, C.-J. Zhao, *Ind. Eng. Chem. Res.* **2009**, *48*, 6992–7003. DOI: 10.1021/ie9004282
[18] D. Cheng, J.-C. Cheng, Y.-M. Yong, C. Yang, Z.-S. Mao, *Chem. Eng. Technol.* **2011**, *34*, 2005–2015. DOI: 10.1002/ceat.201100220
[19] L. Yang, J.-C. Cheng, P. Fan, C. Yang, Z.-S. Mao, *Chem. Eng. Technol.* **2013**, *36*, 443–449. DOI: 10.1002/ceat.201200406
[20] M. Rahimi, S. S. Madaeni, K. Abbasi, *J. Membr. Sci.* **2005**, *255*, 23–31. DOI: 10.1016/j.memsci.2005.01.024
[21] M. Coroneo, G. Montante, J. Catalano, A. Paglianti, *J. Membr. Sci.* **2009**, *343*, 34–41. DOI: 10.1016/j.memsci.2009.07.008
[22] R. Ghidossi, D. Veyret, P. Moulin, *Chem. Eng. Process.* **2006**, *45*, 437–454. DOI: 10.1016/j.cep.2005.11.002
[23] D. E. Wiley, D. F. Fletcher, *Desalination* **2002**, *145*, 183–186. DOI: 10.1016/S0011-9164(02)00406-X
[24] M. Brannock, H. D. Wever, Y. Wang, G. Leslie, *Desalination* **2009**, *236*, 244–251. DOI: 10.1016/j.desal.2007.10.073
[25] M. Brannock, G. Leslie, Y. Wang, S. Buetehorn, *Desalination* **2010**, *250*, 815–818. DOI: 10.1016/j.desal.2008.11.048
[26] D. R. C. Huybrechts, L. De Bruycker, P. A. Jacobs, *Nature* **1990**, *345*, 240–242. DOI: 10.1038/345240a0
[27] L. Meng, H.-Z. Guo, Z.-Y. Dong, H. Jiang, W.-H. Xing, W.-Q. Jin, *Chem. Eng. J.* **2013**, *223*, 356–363. DOI: 10.1016/j.cej.2013.03.049
[28] Z.-X. Zhong, W.-H. Xing, X. Liu, W.-Q. Jin, N.-P. Xu, *J. Membr. Sci.* **2007**, *301*, 67–75. DOI: 10.1016/j.memsci.2007.05.036
[29] Z.-X. Zhong, X. Liu, R.-Z. Chen, W.-H. Xing, N.-P. Xu, *Ind. Eng. Chem. Res.* **2009**, *48*, 4933–4938. DOI: 10.1021/ie801774a
[30] R. J. McDonough, *Mixing for the Process Industries*, Van Nostrand Reinhold, New York **1992**.

